

## Induction charge detector with multiple sensing stages

Manuel Gamero-Castaño<sup>a)</sup>

*Jet Propulsion Laboratory, California Institute of Technology, Pasadena, California 91108*

(Received 18 January 2007; accepted 9 March 2007; published online 11 April 2007)

An induction charge detector yields the net charge and the time of flight of a particle. The unique ability to independently measure these two parameters sets apart this rather simple detection technique. The main shortcoming of this instrument is its high charge detection limit, resulting from the intrinsic noise of the detector electronics and the low signal associated with the charge to measure. The goal of the present work is to lower the detection limit of this detector. This article describes an induction charge detector whose main novelty is a sequence of aligned cylindrical electrodes for measuring the charge of a particle  $n$  times. In a time domain analysis, this feature reduces both the detection limit and the standard error of the charge measurement by factors of  $\sqrt{2}$  and  $\sqrt{n}$ . More importantly, sensing stages could be added to arbitrarily lower the detection limit in a frequency domain analysis. © 2007 American Institute of Physics. [DOI: 10.1063/1.2721408]

### I. INTRODUCTION

Induction charge detectors measure both the total charge and time of flight of a charged particle. The latter yields the charge to mass ratio of the particle if its retarding potential is known. More common detectors like quadrupoles and time of flight techniques, which also provide the charge to mass ratio, are used to infer the charge and mass of simpler particles such as small molecular ions. In this case the lumped nature of mass and charge makes it possible to guess their values with the help of their known ratio. However, these techniques become impractical for more complex particles, including highly charged macromolecules and charged droplets.

A basic induction charge detector, referred to as ICD, consists of a conducting tube aligned with the path of incoming particles. As the particle enters the sensing tube it induces a charge on the tube equal to its own, as long as the tube completely shields the particle from other objects. The charge of the particle can be inferred from the measurement of the tube's electric potential, and the value of its capacitance. The potential signal also displays the entrance and exit of the particle in the tube, conveying its time of flight. If the measurement is done in a vacuum, and the acceleration voltage of the particle is known, the time of flight value is readily converted into the particle's charge to mass ratio or specific charge. It is important to keep in mind that an ICD operating in a vacuum yields the charge and mass of a particle without assumptions about its shape or density, and without perturbing its flight.

It appears that the single sensing tube design was pioneered by Shelton *et al.*,<sup>1</sup> who used it in the 1960s to characterize charged dust particles. Hendricks and collaborators employed the same design to size electrospray droplets, calling it "Faraday cage."<sup>2</sup> Verbitskii *et al.* described a similar design based on two consecutive cylinders, and having a

detection limit of approximately 6200 electron charges.<sup>3</sup> Keaton *et al.* reported an ICD, "charge pick off detector," with a first cylindrical electrode for measuring the charge of the incoming particle, and a second cylinder to determine its time of flight; this device, used for the research of hypervelocity microparticle impact, had a detection limit of approximately 1900 electron charges.<sup>4</sup> Fuerstenau and Benner used a classical Shelton design to study megadalton electrospray ions.<sup>5</sup> They reported a detection limit of 150 electron charges, enabled by a pulse peaking time filtering technique for conditioning the original detector signal. More recently Gamero and Hruby have studied electrospray droplets with a Shelton design.<sup>6</sup> Fuerstenau calibrated the ICD with a test capacitor, which allowed the injection of a known charge level in the cylindrical electrode. Gamero integrated the signal of the detector to compute the charge of the particle.

This article describes a novel ICD with multiple sensing cylinders. We will demonstrate how this design can lower the detection limit of the instrument, down to one electron charge if required. The article is organized as follows: after this introduction, Sec. II describes the geometry and the design principles of the ICD. The calibration technique, the detector noise, and its performance in the time and frequency domains are analyzed in detail. Section III demonstrates the ability of the ICD to characterize complex electrosprays of droplets in vacuum. A succinct summarizing section completes the article.

### II. DETECTOR DESCRIPTION

Figure 1 shows a model of the ICD. The entrance of the detector is a long and narrow channel that limits the number of particles entering the detector, ideally down to one at any given time, and ensures that their trajectories remain close to the detector axis. Downstream of the entrance, and aligned with it, there are eight identical tubes arranged sequentially. The first and last tubes are connected to ground, while the remaining six tubes form a pair of electrodes, sensor 1 and sensor 2, each one having three alternating cylinders. Sensor

<sup>a)</sup>Electronic mail: manuel.gamero@jpl.nasa.gov

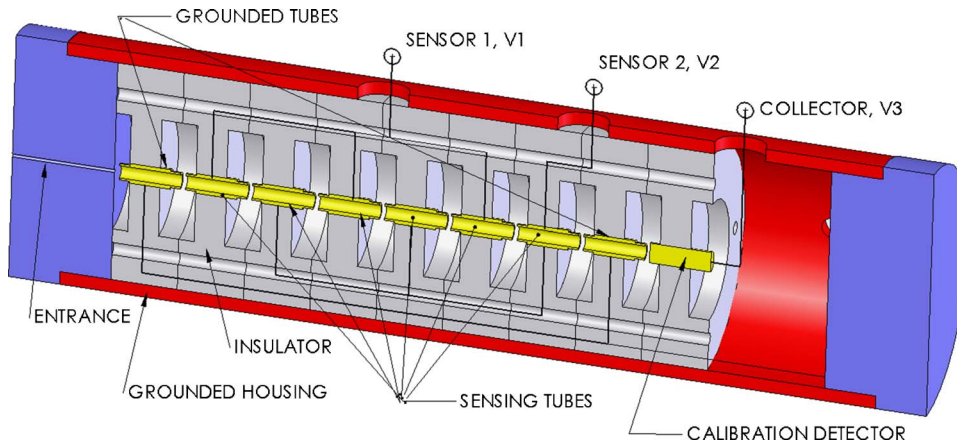


FIG. 1. Section of the induction charge detector.

1 and sensor 2 are the sensing elements of the ICD: when a charged droplet travels across the tubes, the potential difference between the sensors has the shape of a rectangle wave, with an amplitude proportional to the particle's charge and a frequency inversely proportional to its time of flight. The grounded tubes shield the sensing electrodes from the incoming/outgoing particle and increase the sharpness of the leading and trailing edges of the rectangle wave. A final collector electrode receives the charged particle after exiting the sensing electrodes. The collector provides a convenient method for calibrating the ratio between charge and rectangle wave's amplitude and can be eliminated if an alternative calibration technique is employed. Teflon insulators holding the sensing tubes, and a grounded housing tube surrounding all the parts, form the structure of the detector.

Figure 2 is a simplified electrical model of sensor 1 and sensor 2.  $R$  is a 1 G $\Omega$  resistor that provides a path to ground for the input current required by the operational amplifiers, an Analog Devices AD549. Each sensor has an equivalent capacitance with respect to ground, the result of capacitive contributions from sensing tubes, electrical leads, and the stray input capacitance of the operational amplifier. The sources  $V_R$ ,  $V_n$ , and  $I_n$  simulate the Johnson voltage noise of the resistor, and the input voltage and input current noises of the operational amplifier. Sensor 1 and sensor 2 have a mutual capacitance  $C_{12}$ . The electric circuit for the collector

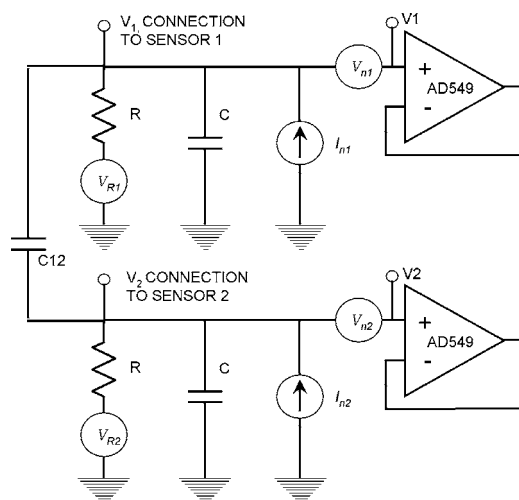


FIG. 2. Simplified model of the detector's electric circuit.

electrode differs by having a smaller 100 M $\Omega$ , 1% resistor (nominal resistance value and tolerance specified by the manufacturer, Ohmite Mfg. Co.).

Figure 3 shows the ICD wave,  $V1-V2$ , and the calibration signal,  $V3-V1$ , generated by the flight of a charged droplet.  $V1-V2$  is a rectangle wave with three cycles, each cycle caused by the passage of the droplet across a pair of alternating sensing tubes. The wave would be symmetric if the capacitances  $C1$  and  $C2$  were identical. We define the time of flight of a particle as the time difference between the leading and trailing edge of the ICD wave,  $t2-t1$ ; the distance traveled by the droplet during this interval is 0.049 m. The charge of the droplet is given by either one of the two following expressions:

$$q_D = \frac{C1C2 + C12C2 + C12C1}{C2} (V1 - V2)_1^*, \quad (1)$$

$$q_D = -\frac{C1C2 + C12C2 + C12C1}{C1} (V1 - V2)_2^*, \quad (2)$$

where  $(V1 - V2)_1^*$  and  $(V1 - V2)_2^*$  are the values of the ICD wave when the particle is at the center of any of the sensing tubes of sensor 1 and sensor 2, respectively. For clarity, these values are shown in Fig. 3. Equations (1) and (2) show that the charge of a particle is proportional to the amplitude of its rectangle wave; the proportionality constant can be computed from known values of  $C1$ ,  $C2$ , and  $C12$ , or from a calibration of  $q_D$  vs  $(V1 - V2)^*$ .

Formulas (1) and (2) require the flux of electric field across the sensing tube ends to be negligible when a particle is located inside the tube, far enough from its ends. The flat tops and bottoms reached by the ICD wave in Fig. 3 indicate that the tubes are indeed long enough to fully shield the particles. Furthermore, we have used the numerical package Maxwell to model a conducting droplet placed in the center of a sensing tube, together with two neighboring tubes. Maxwell computes capacitances between the droplet and the central tube, and between the droplet and neighboring tubes, which have five orders of magnitude ratios. Therefore the electric flux exiting the sensing tube is negligible. Equations (1) and (2) also require electronics that measure  $V1$  and  $V2$  without significant time distortion, i.e., the cut off frequency of the electronics needs to be significantly higher than the frequency of the ICD wave.

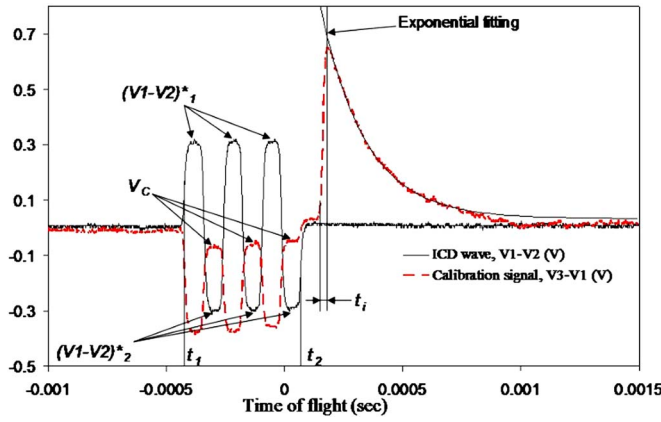


FIG. 3. Detector signals associated with the flight of a charged droplet.

The calibration signal  $V3-V1$  exhibits two interesting features. First,  $V3-V1$  has an offset from zero when the particle is inside any of the tubes of sensor 2; this offset is caused by the capacitive coupling between sensor 1 and sensor 2, and its value is

$$V_C = \frac{C_{12}}{C_1} (V_1 - V_2)_2^* \quad (3)$$

Second, the arrival of the particle to the collector electrode induces a sharp increase in its potential, followed by an exponential decay with a time constant equal to  $C_3R_3$ . To compute the relation between the values of this voltage peak and the particle's charge, we write the differential equation for the collector potential

$$\frac{dV_3}{dt} + \frac{V_3}{R_3C_3} = \frac{I_D[t]}{C_3}, \quad V_3[0] = 0, \quad (4)$$

where  $I_D[t]$  is the electrical current induced in the collector electrode by the arriving particle. If the characteristic time associated with the induction of current,  $t_I$ , is much smaller than  $C_3R_3$ ,  $I_D[t]$  can be modeled by an impulse-like function with area equal to  $q_D$ , but whose actual shape is of little importance to compute  $V_3$  at  $t \geq t_I$ . Since our estimates for  $t_I$  and  $C_3R_3$  in Fig. 3 are 29 and 190  $\mu\text{s}$ , respectively, we can take advantage of this, and model  $I_D[t]$  with, for example, a rectangle function. The solution for  $V_3[t]$  then becomes

$$I_D[t] = \frac{q_D}{t_I} (H[t] - H[t - t_I]), \quad (5)$$

$$V_3[t] = \frac{q_D R_3}{t_I} \begin{cases} 1 - e^{-\frac{t}{R_3C_3}}, & 0 \leq t \leq t_I \\ \frac{t_I}{(e^{\frac{t_I}{R_3C_3}} - 1)} e^{-\frac{t}{R_3C_3}}, & t > t_I \end{cases}, \quad (6)$$

$V_3[t]$  has a maximum at  $t=t_I$ , when the charge particle collides with the collector electrode. The value of this maximum for small  $t_I/R_3C_3$  is

$$V_3^* = \frac{q_D}{C_3} \left( 1 - \frac{1}{2} \frac{t_I}{R_3C_3} \right) + O\left( \frac{t_I}{R_3C_3} \right)^2. \quad (7)$$

As expected, the capacitance  $C_3$  is the ratio between  $q_D$  and  $V_3^*$  only when  $t_I \ll C_3R_3$ . Alternatively, for small but finite values of  $t_I/R_3C_3$ , one can use the first order correction in Eq. (7) to compute  $q_D$  accurately.

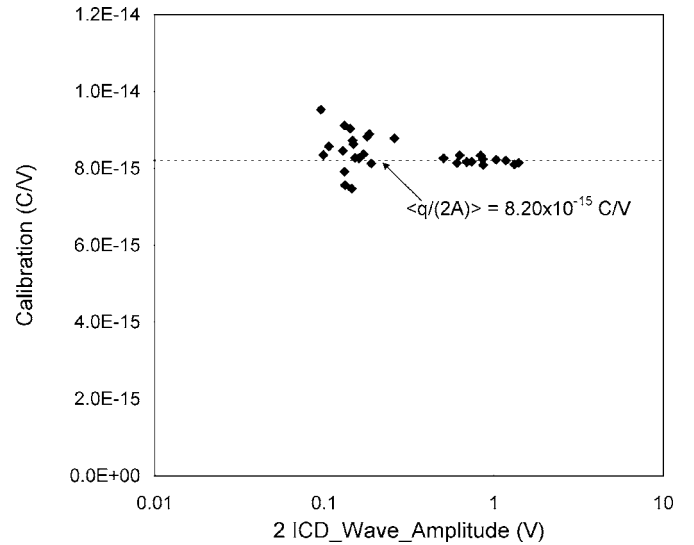


FIG. 4. Detector signal vs charge calibration.

Figure 3 also shows an exponential fitting to the decaying side of the collector potential peak. The exponential fitting yields a time constant  $C_3R_3 = 190 \mu\text{s}$ , which translates into a value of  $1.9 \times 10^{-12} \text{ F}$  for  $C_3$ . Extending this analysis to a sample of 12 droplets, we compute an average value  $\langle C_3 \rangle = 2.03 \times 10^{-12} \text{ F}$ , with a standard deviation of  $1.4 \times 10^{-13} \text{ F}$ .

The calibration  $\Lambda$  of the detector, or ratio  $q_D / \langle (V_1 - V_2)_1^* - (V_1 - V_2)_2^* \rangle$ , is computed with  $\langle C_3 \rangle$ , Eq. (7), and the mean of  $(V_1 - V_2)_1^* - (V_1 - V_2)_2^*$  for the three cycles of the ICD wave. Figure 4 shows  $\Lambda$  for 30 droplets as a function of  $\langle (V_1 - V_2)_1^* - (V_1 - V_2)_2^* \rangle$ . The droplet charges cover the range ( $8.29 \times 10^{-16} \text{ C}$ ,  $1.14 \times 10^{-14} \text{ C}$ ). The calibration shows a larger variance for the smaller droplets, mostly because the calibration signal, being noisier than the ICD signal, introduces larger errors in  $\Lambda$  for the smaller charge values. Because of this, we use only the set of 12 larger droplets around  $(V_1 - V_2)_1^* - (V_1 - V_2)_2^* = 1 \text{ V}$  to compute the mean of the calibration ratio,  $\langle \Lambda \rangle = 8.20 \times 10^{-15} \text{ C/V}$ , with a standard deviation of  $8.3 \times 10^{-17} \text{ C/V}$ . The steady state gain of the amplifiers connected to sensor 1, sensor 2, and the collector electrode is 273 (this value is derived from the specifications of the instrumentation amplifier and resistive networks used in the circuit).

We can now compute the capacitances  $C_1$ ,  $C_2$ , and  $C_{12}$  with  $\langle \Lambda \rangle$  and Eqs. (1)–(3). From the signals shown in Fig. 3, we have  $\langle (V_1 - V_2)_1^* \rangle = 0.296 \text{ V}$ ,  $\langle (V_1 - V_2)_2^* \rangle = 0.3121 \text{ V}$ ,  $\langle V_C \rangle = -0.056 \text{ V}$ , and  $q_D = 4.98 \times 10^{-15} \text{ C}$ . The values of the capacitances are  $C_1 = 3.36 \times 10^{-12} \text{ F}$ ,  $C_2 = 3.19 \times 10^{-12} \text{ F}$ , and  $C_{12} = 6.03 \times 10^{-13} \text{ F}$ . The numerical values computed by Maxwell are  $1.59 \times 10^{-12} \text{ F}$  for the capacitance with respect to ground of the three tubes of either sensor 1 or sensor 2, and  $5.79 \times 10^{-13} \text{ F}$  for their mutual capacitance. It should not surprise that the experimental values for  $C_1$  and  $C_2$  are larger than  $1.59 \times 10^{-12} \text{ F}$ , because the latter needs to be increased with the stray input capacitances of the operational amplifier attached to the sensors (an unknown quantity of the order of  $10^{-12} \text{ F}$ ), and the capacitance of electrical leads. On the other hand, the experimental estimate for  $C_{12}$  is similar

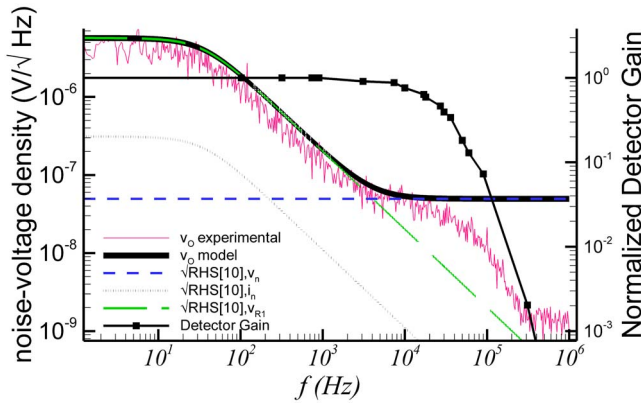


FIG. 5. Experimental and model noise of the detector.

to the numerically computed  $5.79 \times 10^{-13}$  F value because no significant parasitic capacitances contribute to C12.

We now use the noise model shown in Fig. 2 to calculate the input-referred noise of the rectangle wave signal. As mentioned before,  $V_R$  is a voltage source simulating the Johnson noise of the input resistors, while  $V_n$  and  $I_n$  are the input voltage and input current noises of the amplifier. The square root of their power spectral densities per unit time are  $v_R$ ,  $v_n$ , and  $i_n$ . For simplicity, we will take C1 and C2 to be equal, C. The voltage difference between the inputs of the amplifiers is given by

$$V_O = V_1 - V_2 = V_1 - V_2 + V_{n1} - V_{n2}, \quad (8)$$

$$\frac{d(V_1 - V_2)}{dt} + \frac{V_1 - V_2}{R(C + 2C12)} = \frac{V_{R1} - V_{R2}}{R(C + 2C12)} + \frac{I_{n1} - I_{n2}}{(C + 2C12)}. \quad (9)$$

After taking the Fourier transform of Eq. (9), and adding the square of the voltage amplitudes, the input referred power spectral density per unit time  $v_O^2$  is

$$v_O^2 = 2v_n^2 + \frac{2v_R^2}{1 + [2\pi R(C + 2C12)f]^2} + \frac{2R1^2 i_n^2}{1 + [2\pi R(C + 2C12)f]^2}. \quad (10)$$

The data sheets of the amplifier AD549 tabulate typical values for  $i_n$ ,  $2.2 \times 10^{-16}$  A/ $\sqrt{\text{Hz}}$ , and  $v_n$ ,  $3.5 \times 10^{-8}$  A/ $\sqrt{\text{Hz}}$ . The expression for the resistive Johnson noise density is  $v_R \sqrt{4kTR}$  V/ $\sqrt{\text{Hz}}$ .

Figure 5 shows the experimental and model values for  $v_O$ , together with the square root of each term in the right-hand side of Eq. (10). The experimental  $v_O$  is the square root of the one-sided power spectral density per unit time of the signal  $V_1 - V_2$ , divided by the detector dc gain to allow an input-referred comparison. Figure 5 shows a good agreement between the noise model and the measured noise for frequencies smaller than approximately 30 kHz. The disagreement beyond 30 kHz is due to the deterioration at high frequency of the open loop gain of the operational amplifiers. This causes attenuation of the amplified signal, or equivalently the reduction of the detector gain. The gain of the detector, nor-

malized with its 273 dc value, is plotted in Fig. 5 as well. The gain shows an accelerated degradation beyond 30 kHz. For simplicity we will consider that the detector has a bandwidth of 30 kHz, within which its gain can be regarded as constant and equal to 273. Figure 5 and Eq. (10) show that the input voltage noise of the AD549 op-amp sets a minimum value for the detector noise at high frequencies. At lower frequencies, resistive Johnson noise dominates. For the values of C and R of our detector, Johnson noise and  $v_n$  become comparable at approximately  $f=4$  kHz. The voltage noise associated with  $I_n$  is always negligible because of the low input current noise of the operational amplifier and the particular value of R.

The root-mean-square amplitude  $V_{\text{rms}}$  of the ICD signal in the absence of charged particles is the background noise of the detector. We will use this figure to estimate the charge detection limit of the ICD. According to Parseval's theorem, the  $V_{\text{rms}}$  measured in a bandwidth  $[f1, f2]$  is

$$V_{\text{rms}} = \sqrt{\int_{f1}^{f2} \text{PSDT}[f] df}, \quad (11)$$

where PSDT[f] stands for the one-sided power spectral density per unit time of the signal.<sup>7</sup> In our measurements, a pair of sampling parameters fixes the bandwidth limits; for example, if the time of flight (TOF) of a particle across the detector and the sampling rate  $\tau$  are chosen, the bandwidth is  $[1/\text{TOF}, 1/2\tau]$ ; alternatively, if the TOF and the number (#) of sampled points per cycle are chosen, the bandwidth becomes  $[1/\text{TOF}, \#n/2\text{TOF}]$ , where  $n$  is the number of cycles of the ICD wave. Figure 6 plots the root-mean-square amplitude of our three-cycle ICD as a function of the time of flight, for different sampling rates and sampled points per cycle. Figure 6 also shows the minimum possible noise of the ICD, computed with the input voltage noise of the AD549 amplifier. The upper bound associated with the sampling rate  $\tau=16.7 \mu\text{s}$  is somehow arbitrary, and corresponds to our definition of the detector bandwidth, 30 kHz. Figure 6 shows that for typical operating conditions (for example, the square wave in Fig. 3 has a time of flight of 493  $\mu\text{s}$ ), the ICD has a  $V_{\text{rms}}$  of the order of 2 mV, or equivalently 103 electrons. It is worth noticing that in the limiting case of a constant noise density, the root-mean-square amplitude is roughly proportional to  $\sqrt{f2}$ , and reducing the sampling rate while increasing the time of flight of the particle lowers considerably the noise of the detector. The implementation of this strategy requires the extension of the lower end of the frequency band in which the detector noise is equal to its minimum value given by  $v_n$ . This can be achieved by increasing the detector input impedance. The improved background noise associated with this scenario is illustrated in Fig. 6 by the region within dotted lines.

Our ICD features three rectangle wave cycles because this periodical signal enhances the accuracy of the ICD. The simplest ICD has a single sensing tube, and the flight of a charged particle through it generates a rectangle function. Additional sensing tubes bring about the following improvements:

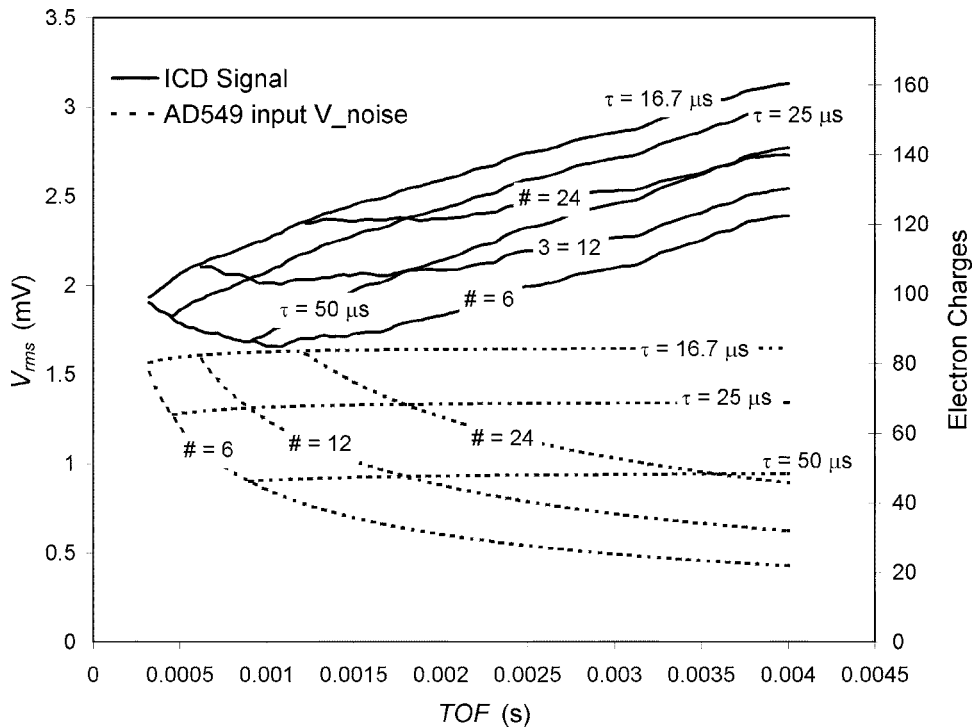


FIG. 6. Charge detection limit in time domain analysis.

- (1) A second tube, whose signal is subtracted from that of the first tube, increases the signal to noise ratio by a factor of  $\sqrt{2}$  (the new signal and its noise are larger than the originals by a factor of 2 and  $\sqrt{2}$ , respectively), and completes one cycle of a rectangular wave.
- (2) Additional sensing tube pairs, connected as shown in Fig. 1, increase proportionally the number of independent measurements of the particle's charge. Therefore, both a mean value and its standard error,  $\sigma/\sqrt{n}$ , can be defined and computed for the charge, where  $\sigma$  and  $n$  stand for the standard deviation of the sample and the number of samples (i.e., wave cycles).
- (3) The number of sensing tubes connected to one operational amplifier cannot be increased limitlessly without penalizing the sensitivity of the detector. Each sensing tube increases the net capacitance of the amplifier, which is inversely proportional to its sensitivity. Because any operational amplifier has an intrinsic capacitance (approximately  $10^{-12}$  F for our AD549), one should limit the number of sensing tubes so that their equivalent capacitance does not exceed that of the amplifier. We have used three sensing tubes per operational amplifier because the capacitance of each tube is approximately  $5.3 \times 10^{-13}$  F. As hinted by Eq. (10), the restriction of the numbers of sensing tubes attached to an operational amplifier can be relaxed when Johnson noise is the major contributor to the noise of the detector.
- (4) A pair of operational amplifiers, each one with an optimum number  $k$  of sensing tubes, makes an ICD sensing block. One can arrange  $m$  ICD blocks in series, and record each block's output independently, to further reduce the standard error of the charge measurement,  $\sigma/\sqrt{k \times m}$ . This strategy is especially beneficial for particles with a charge value near the detection limit of the ICD.

As mentioned in item (2), a larger number of sensing stages does lower the standard error of the charge measurement. This translates in an improvement on the signal to noise ratio

$$\text{SNR}_T = \frac{A\sqrt{n}}{V_{\text{rms}}}, \quad (12)$$

where  $A$  is the amplitude of the ICD wave. Since the particle's charge remains constant throughout its  $n$  samplings, the root-mean-square amplitude of the ICD signal is a good estimate of the standard deviation of the sample. Unfortunately, adding sensing stages does not lower the charge detection limit of the ICD in this time domain analysis, because a signal with an amplitude of the order of the detector's  $V_{\text{rms}}$  is needed to distinguish the particle's rectangle wave pattern from the background noise.

The earlier constraint on the charge detection limit is removed when the analysis is carried out in the frequency domain. To demonstrate this we notice that the Fourier transform of a rectangle wave signal is given by

$$R(f) = \frac{Ai}{\pi f} \left[ \frac{1 - e^{2n2\pi\Delta fi}}{2} + \sum_{k=1}^n (e^{2k2\pi\Delta fi} - e^{(2k-1)2\pi\Delta fi}) \right], \quad (13)$$

where  $A$ ,  $\Delta$ , and  $n$  are the amplitude, half-period and number of cycles of the rectangle wave, respectively.  $f$  stands for frequency, in Hertz units. For a time window equal to the time of flight of the particle, the one-sided power spectral density per unit time of the rectangle wave is

$$\text{PSDT}_R(f) = \frac{2|R(f)|^2}{2n\Delta}, \quad (14)$$

This function has an absolute maximum at  $f^* = (1/2\Delta)(1 - \varepsilon[n])$ , surrounded by additional local maxima.

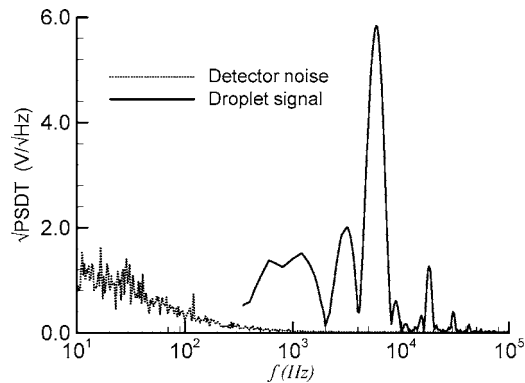


FIG. 7. Signal associated with a droplet and detector background noise in the frequency domain.

$\varepsilon$  is a small positive quantity that approaches zero for increasing  $n$ ; the approximate values of  $\varepsilon$  for  $N=2, \dots, 6$  are 0.085, 0.035, 0.019, 0.012, and 0.0085. The maximum value of the square root of the power spectral density is

$$P^* = \sqrt{\text{PSDT}(f^*)} = \frac{4A}{\pi} \sqrt{n\Delta(1 + \alpha[n])}. \quad (15)$$

The approximate values of  $\alpha$  for  $N=2, \dots, 6$  are 0.041, 0.017, 0.0097, 0.0062, and 0.0042.  $P^*$  is proportional to the amplitude of the particle's rectangle wave, and therefore it is proportional to its charge. Thus, we will use Eq. (15) as the signal associated with the charge of a particle in the frequency domain analysis. The expression for  $P^*$  shows that increasing the time of flight of the particle, which can be done by adding sensing stages or slowing the particle, increases the charge signal. Since the measurement noise, given by the square root of the PSDT of the ICD signal in the absence of particles, can be made independent of either  $n$  or  $\Delta$ , increasing  $n$  and/or  $\Delta$  does lower the detection limit of the ICD. In principle,  $n$  and/or  $\Delta$  can be increased enough to reach a detection limit of one electron.

Figure 7 illustrates the frequency domain analysis. The function  $\sqrt{\text{PSDT}_R(f)}$  for the ICD wave of Fig. 3 has an absolute maximum  $P^* = 5.836$  mV/Hz at  $f^* = 5888$  Hz. Using the expressions for  $f^*$  and  $P^*$ , we obtain values of 492  $\mu\text{s}$  and  $4.71 \times 10^{-15}$  C for the time of flight and the charge of the particle. They compare well with the time domain values of 493  $\mu\text{s}$  and  $4.98 \times 10^{-15}$  C. The lower frequency domain charge is likely caused by the finite rise and fall times of the ICD wave edges resulting in a smaller maximum  $P^*$  for the smoother wave. This inaccuracy can be eliminated by calibrating the detector in the frequency domain, just like it was done in the time domain analysis. The background noise at  $f^* = 5888$  Hz is 0.018 mV/Hz or, equivalently, 91 electrons. Furthermore, if the detector noise were made equal to its minimum possible value  $v_n$ , e.g., by using a larger input resistor, the background noise would be some 48 electrons.

### III. CHARACTERIZATION OF AN ELECTROSPRAY

We have used the ICD to analyze the electrospays of a solution of 1-ethyl-3-methylimidazolium bis(trifluoromethylsulfonyl) imide in propylene carbonate. A typical electro-spray source operating in vacuum is described elsewhere.<sup>6</sup>

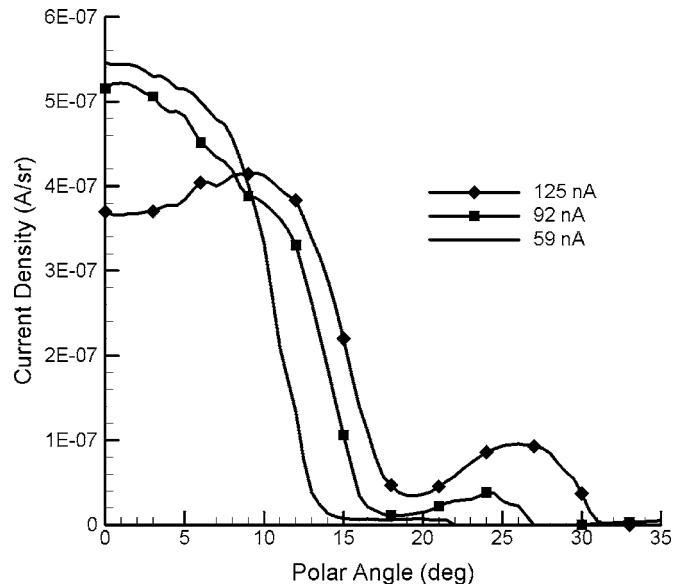


FIG. 8. Beam current profiles associated with three electrospays.

Figure 8 shows the current density of the beam as a function of the polar angle with respect to the beam axis, for three different beam currents. The beam is relatively narrow for the lowest current, and broadens as the current increases. The 125 and 92 nA sprays display two coaxial beams, with a region in between fairly depleted of droplets. This dichotomy is caused by the generation of main and satellite droplets at the electro-spray jet breakup, which starts when a high enough propellant flow rate, or equivalently beam current, is exceeded.<sup>6</sup> The satellite droplets have smaller mass, mass to charge ratio, and retarding potential than the main droplets, and accordingly are preferentially pushed outward by the spray's space charge. Figure 9 shows diameter distributions for the 92 nA electro-spray, taken at different polar angles. Each diameter distribution has been computed with approximately 200 droplet records measured by the ICD. The distribution is broadest at the axis of the beam, where only main droplets are present. For increasing polar angle, but still within the inner core populated by main droplets, the diam-

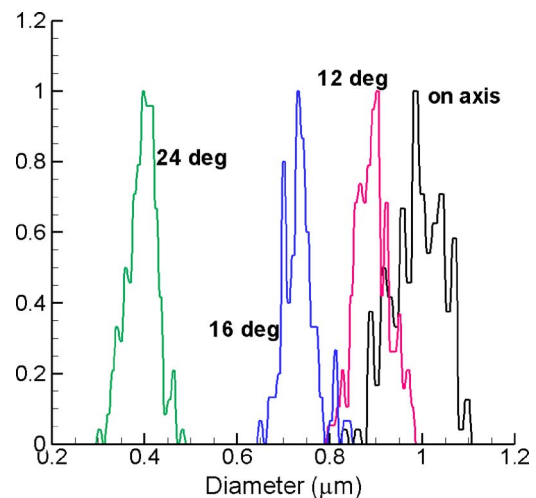


FIG. 9. Electro-spray droplet diameter distributions at different beam polar angles.

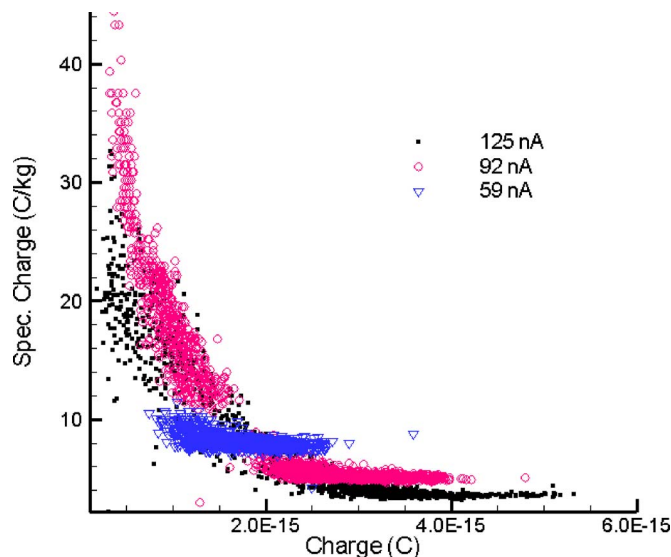


FIG. 10. Charge to mass ratio vs charge of electro-spray droplets.

eter distributions become narrower and the mean diameter smaller. The mean diameter falls much faster for still larger polar angles, and the outer beam associated with satellite droplets develops. Figure 10 shows the droplets' charge to mass ratio versus charge for the three beam currents. The droplets have been sampled throughout the whole polar angle range of the beams. Each spray has a wide charge window within which the droplet's mass to charge ratio is roughly constant and the variation of specific charge between droplets with equal charge is small. This quasicontant specific charge region is associated with main droplets. Figure 10 also shows the higher specific charges, and larger variability, of the satellite droplets in the 125 and 92 nA electro-sprays.

#### IV. CONCLUSION

Multiple sensing stages improve the performance of a charge capacitive detector. Our design generates a rectangle wave with three cycles as a response to the flight of a particle through it. When compared to an ICD with a single sensing cylinder, the periodical signal lowers the charge detection limit in the time domain analysis by a factor of  $\sqrt{2}$ . In addition, the  $n$ -periodical signal amounts to  $n$  independent measurements of the particle's charge, which increases the signal to noise ratio by a factor of  $\sqrt{n}$  by reducing the standard error of the charge measurement.

The periodical signal leads naturally to its analysis in the frequency domain. In this case the detection limit can be lowered without bound, by increasing the number of periods of the signal and/or lowering the speed of the particle. In principle, a particle holding one electron charge could be measured with a modified design of this ICD.

The background noise of the detector depends on whether a time or frequency domain analysis is followed. For the former, the noise mostly depends on the measurement sampling frequency. For the latter, the noise is a function of the frequency of the ICD wave. It is always important to minimize the background noise density of the ICD electronics. In our particular design, this is best accomplished by extending to lower frequencies the area in which the operational amplifier's input voltage noise becomes comparable to the Johnson noise of the input resistor. As a reference, our three cycle ICD has demonstrated a charge noise of approximately 100 electrons, in the typical measurement of a droplet with a time of flight of 493  $\mu\text{s}$ .

In general, increasing without limit the number of sensing cylinders connected to one operational amplifier does not improve the frequency domain's charge detection limit, or the time domain's charge standard error. The reason for this is the proportional decrease of the sensor sensitivity due to the increase of its input capacitance. This problem can be solved by sequencing ICD sensing blocks, each one having a pair of operational amplifiers and an optimum number of cylinders, and recording independently the outputs of each sensing block.

#### ACKNOWLEDGMENTS

I am indebted to Dr. I. Katz for many suggestions and ideas. The research described in this article was carried out at the Jet Propulsion Laboratory, California Institute of Technology, under a contract with the National Aeronautics and Space Administration.

- <sup>1</sup>H. Shelton, C. D. Hendricks, and R. F. Wuerker, *J. Appl. Phys.* **31**, 1243 (1960).
- <sup>2</sup>J. J. Hogan and C. D. Hendricks, *AIAA J.* **3**, 296 (1965).
- <sup>3</sup>S. S. Verbitskii, I. S. Grabovskii, V. E. Zhuraviev, A. K. Kulebyakin, and A. A. Malyutin, *Prib. Tekh. Eksp.* **4**, 221 (1989).
- <sup>4</sup>P. W. Keaton *et al.*, *Int. J. Impact Eng.* **10**, 295 (1990).
- <sup>5</sup>S. D. Fuerstenau and W. H. Benner, *Rapid Commun. Mass Spectrom.* **9**, 1528 (1995).
- <sup>6</sup>M. Gamero-Castaño and V. Hruba, *J. Fluid Mech.* **459**, 245 (2002).
- <sup>7</sup>W. H. Press, S. A. Teukolsky, W. T. Vetterling, and B. P. Flannery, *Numerical Recipes in C*, 2nd ed. (Cambridge University Press, Cambridge, 1995), Chap. 12.